

Design and Force Performance Analysis of a Climbing Robot Based on Halbach Magnetic Array

Hua Zhong^a, Deshu Wang^{b,c}, Junjie Gong^{b,c}, Caixia Ban^{b,c}, Wei Wei^{b,c*}, Yu Long^{b,c}

^aGuangxi Road and Bridge Engineering Group Co., Ltd, Nanning 530200, China

^bState Key Laboratory of Featured Metal Materials and Life-cycle Safety for Composite Structures, Guangxi University, Nanning, 530004, China

^cSchool of Mechanical Engineering, Guangxi University, Nanning 530004, China

Received 5 Jul 2024

Accepted 13 Oct 2024

Abstract

Dangers in aerial work will cause huge economic losses and casualties. To improve this problem, this paper designs a track climbing robot based on the Halbach square magnetic array, which can be used for the inspection and maintenance of large steel structures. First, the adsorption unit uses the Halbach square magnetic array to arrange permanent magnets. The load-bearing mechanism transfers the weight of the robot body to the track plate while sharing the load of two axes and assisting the track to stick to the wall. The tensioning mechanism is used to support the track. Then, the critical states of the two failure types of sliding and overturning of the climbing robot are analyzed, and the magnetic adsorption force provided by the single track plate required for the stable adsorption of the robot is determined; the two motion states of the robot, straight and turning, are analyzed, and the torque provided by the drive device required when the robot moves is determined. Finally, the adsorption force of the adsorption unit is calculated by COMSOL simulation; the axial and circumferential movement of the track along the curved surface is simulated and analyzed to verify the feasibility of the climbing robot. The results show that the robot can be stably adsorbed on the wall, the adsorption force of a single track shoe should be no less than 48.59N for the robot to move flexibly on the wall, and the driving torque provided by the drive device of the single-side track should be greater than 20.47N, the adsorption unit using N42 permanent magnet can bring an adsorption force of 27.812N.

© 2024 Jordan Journal of Mechanical and Industrial Engineering. All rights reserved

Keywords: Climbing robot, Permanent magnet adsorption, Track, Halbach square array.

1. Introduction

High-altitude operations are highly prone to significant accidents, resulting in considerable economic losses and casualties [1]-[3]. To mitigate these risks, the use of climbing robots to replace manual labor in such tasks is crucial [4]. However, current climbing robots face challenges such as poor load-bearing capacity, high environmental requirements for wall surfaces, heavy weight, and high energy consumption[5].

There are three primary types of climbing robots: bionic, negative pressure, and magnetic adhesion. Bionic climbing robots draw design inspiration from the climbing mechanisms of insects or animals. Mark et al.[6]-[10] developed the Stickybot, a gecko-inspired robot with four flexible feet made from anisotropic adhesive materials, enabling it to climb various vertical surfaces. Guan et al.[11]-[15] designed the Climbot, a modular inchworm-inspired climbing robot with strong flexibility and maneuverability, capable of climbing various rod-like structures and overcoming obstacles. Xu et al.[16], inspired by the adhesion characteristics of flies and gobies, proposed a climbing robot with ratchets, capable of climbing within a

0-360 degree range under a maximum load of 0.5 kg. Chen et al. [17][18] introduced a gecko-inspired climbing robot based on a vibration suction cup, which uses a negative pressure technique called vibration suction, achieving a maximum vertical climbing speed of 13.75 mm/s and a maximum turning angle of 20°. Liu et al. [19][20], inspired by the oriental silk moth (*SericorientalisMotschulsky*), developed a tracked climbing robot with bionic spines, capable of climbing on sandpaper, bricks, rough plaster, and pebble walls. In 2021, the Hong Kong Polytechnic University [21] designed a soft rigid pipe climbing robot for safety inspection on the pipe network with uncertain obstacles, which can hold pipes of different diameters with controllable adhesion. With no load, the robot is able to climb at a rapid speed of 1.09m/s, with a maximum speed of 0.828m/s when carrying a 500g load. Despite these advancements, bionic climbing robots often suffer from slow climbing speeds, poor load capacity, and high costs associated with the design and manufacture of bionic mechanisms and materials[22-23].

Negative pressure climbing robots rely primarily on pressure differentials to firmly adhere to wall surfaces, offering good adhesion capabilities and wide applicability. Yoshida et al. [24] designed a climbing robot using passive

* Corresponding author e-mail: gongjj95@qq.com, weiwei@gxu.edu.cn.

suction cups as attachment devices, requiring no additional energy to maintain adhesion and achieving climbing with low energy consumption. Cao et al. [25] proposed a rolling-adsorption wall climbing robot (RWCR), capable of bearing loads up to 6.2 kg on smooth glass walls and up to 4.2 kg when moving laterally. However, these robots demand high wall surface flatness, and cracks can cause suction cup air leaks, reducing adhesion and load capacity, and potentially leading to falls. Zhao et al. [26] introduced the Vortexbot, featuring a suction device utilizing vortices to generate suction, maintaining adhesion without direct wall contact, even on rough surfaces or obstacles. Liu et al. [27] designed a climbing robot using a vortex fan to create pressure differentials, similar to a centrifugal pump, achieving a maximum speed of 7.11 cm/s and a maximum load of 1 kg. However, this method generates significant noise and requires extra energy for negative pressure creation, increasing system energy consumption.

Magnetic adhesion methods require lower wall surface flatness and are less affected by cracks. Song et al. [28] designed a permanent magnet adhesion wheeled climbing robot, with a prototype weight of 97 kg, a maximum effective load of 62.9 kg, and an average speed of 4 m/min, capable of overcoming 6 mm high obstacles. Magnetic wheel climbing robots can achieve wall adhesion and movement, but variations in wall thickness or surface curvature can cause changes in air gaps, leading to insufficient adhesion. Thungod et al. [29] designed an adaptive electromagnetic adhesion mechanism for magnetic wheel-based curved surface climbing robots, utilizing a PID controller to adjust electromagnetic force, providing flexible adhesion on ferromagnetic curved surfaces [30]-[34].

Magnetic adhesion includes electromagnetic and permanent magnetic adhesion. Electromagnetic adhesion maintains adhesion through a magnetic field generated by electromagnetic coils, requiring a continuous power supply. Permanent magnetic adhesion generates adhesion through the magnetic field of permanent magnets, requiring no power supply and offering high stability. Due to the lack of continuous energy consumption, permanent magnetic adhesion is more energy-efficient compared to electromagnetic adhesion. Tao et al. [35][36] designed a permanent magnet adhesion climbing robot, with a prototype weight of 74 kg, capable of bearing an effective load of 173 kg without slipping in a static state. Gao et al. [37] designed a climbing robot utilizing tracks with multiple magnetic adhesion units, weighing 7.5 kg and measuring 430×145×234 mm, capable of carrying a 10 kg load and overcoming 10 mm obstacles on vertical walls. Magnetic adhesion provides significantly greater adhesion force than other methods, enabling climbing robots to have a stronger load-bearing capacity [38][39].

However, permanent magnetic adhesion often uses chain drives and requires many permanent magnets, resulting in heavy robot weight. Zhang et al. [40, 41] proposed a tracked wall-climbing robot suitable for ship wall characteristics, consisting of two passive adaptive track mechanisms and a connecting module, employing a Halbach array to reduce robot weight. This robot can achieve adaptive curvature movement and has a certain load-bearing capacity. However, the permanent magnets are installed inside the tracks, causing variations in the distance

between the magnets and the wall, significantly impacting adhesion force stability.

This paper presents the design of a tracked climbing robot based on a Halbach rectangular magnetic array. The adsorption units employ a Halbach square magnetic array to arrange the permanent magnets, achieving greater adsorption force with fewer magnets, thereby reducing the robot's weight. The designed load-bearing mechanism transmits the robot's gravity to the track plates, sharing the two-axis load, enhancing load capacity, and assisting the tracks in adhering to the wall. The designed tensioning mechanism supports the tracks, reducing energy loss caused by slack and vibration of the non-contacting track segments.

2. Structural Design of the Climbing Robot

The structure of the climbing robot designed in this study is illustrated in Figure 1. To enhance the robot's flexibility, both the front and rear wheels can function as drive wheels. A cross-pin universal joint is employed between the drive wheels and the drive device to allow the tracks on both sides of the robot to adjust their position and better conform to the wall surface. For lightweight construction, a toothed drive system is utilized, where the drive wheel's gear teeth engage with the track plate's drive holes to transmit motion.

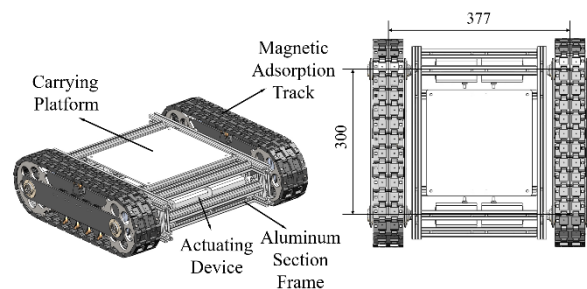


Figure 1. Structure of the climbing robot.

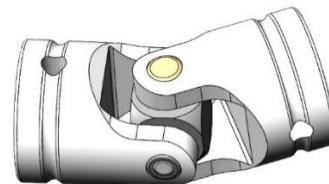


Figure 2. Cross-pin universal joint.

2.1. Design of the Adsorption Structure

Given the need for the climbing robot to operate on curved surfaces, permanent magnets are installed on the track plates to maintain a consistent distance from the wall, thereby ensuring stable adsorption force.

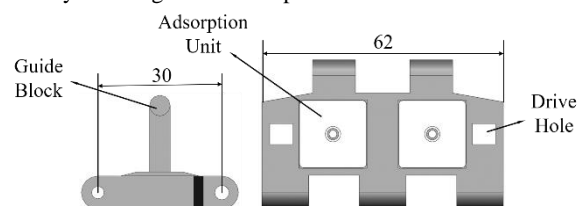


Figure 3. Structure of the trackplate.

The trackplate of the climbing robot, shown in Figure 3, consists of track plates and adsorption units. Each

adsorption unit contains an embedded nut connect to the track plates via screws. To minimize magnetic leakage and maximize the use of the magnets' magnetic energy, the adsorption units employ a Halbach rectangular magnetic array.

A single permanent magnet adsorption unit is depicted in Figure 4, where the arrows indicate the magnetization direction of the permanent magnets. During climbing, the adsorption units move with the track plates, continually adhering to and detaching from the curved wall surface, which inevitably leads to collisions and friction. To protect the permanent magnets within the adsorption units from damage, protective casings are used.

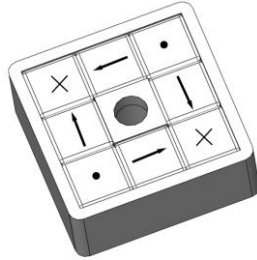


Figure 4. Structure of an adsorption unit.

2.2. Design of the Track Load-Bearing Mechanism

When the robot is positioned on the upper part of a wall, the tracks' two axles bear the robot's weight. Conversely, when the robot is on the lower part of the wall, the hinged connections between the track plates, torque cannot be transmitted between track plates, causing the weight-induced overturning torque to act primarily on the track plates at both ends of the contact section with the wall. In this scenario, many adsorption units cannot function effectively against the overturning torque [9]-[11].

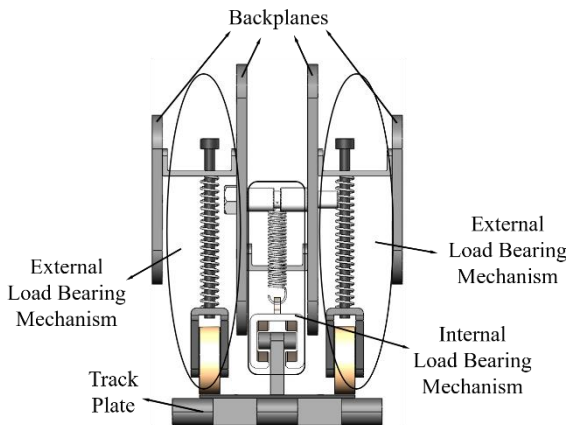


Figure 5. Load-bearing mechanism.

To address this issue, a load-bearing mechanism as shown in Figure 5 is proposed. This mechanism consists of internal and external parts. The internal load-bearing mechanism transfers the overturning torque caused by the robot's weight to the track plates in contact with the wall and limits the lateral displacement of the track plates. When the robot is on the lower part of the wall, this mechanism helps the track resist the overturning torque. The external load-bearing mechanism primarily distributes the forces of the two axles on the tracks. When the robot is on the upper part of the wall, a portion of the robot's weight is directly transferred to the tracks via this mechanism, reducing the

load on the axles. Additionally, the external mechanism assists the tracks in adhering to the wall, aiding in obstacle traversal.

The internal load-bearing mechanism is divided into six segments, each consisting of fixed bolts, tension springs, limit plates, and load-bearing guide slots. Fixed bolts attach the robot's main frame to the tension springs, which transfer the robot's weight to the connected load-bearing guide slots. Limit plates constrain the position of the guide slots. The guide slots feature T-shaped grooves, allowing the guide blocks on the track plates to slide within them, restricting lateral displacement and transferring the robot's weight to the track plates in contact with the wall. When the robot is on the lower part of the wall, the overturning torque due to the robot's weight is distributed across all contact track plates. The contact surfaces of the guide blocks' protrusions in the T-shaped grooves are curved to compensate for vertical misalignment when the tracks bend while climbing over curved surfaces or obstacles, ensuring smooth passage of the guide blocks through the segments of the internal load-bearing mechanism.

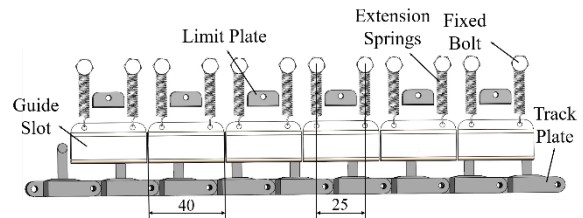


Figure 6. Internal load-bearing mechanism.

The external load-bearing mechanism comprises compression springs, baffles, rubber-coated rollers, and guide bolts. Baffles fixed to the robot's main frame transfer the robot's weight to the compression springs, which then transfer the force to the rubber-coated rollers, which in turn apply the force to the tracks. This arrangement reduces the load on the axles and assists in maintaining track adhesion to the wall when traversing obstacles. The guide bolts restrict the deformation of the compression springs and prevent the springs from failing due to bending. Additionally, the bolts limit the rotation of the rubber-coated rollers, preventing them from slipping and reducing friction.

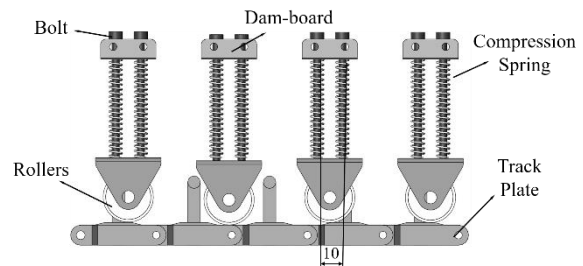


Figure 7. External load-bearing mechanism.

2.3. Design of the Tensioning Mechanism

When the tracks adhere to the wall, the sections between the wheels not in contact with the wall tend to sag due to gravity, causing vibration and energy loss during movement. The track tensioning mechanism, as shown in Figure 8, is designed to prevent sagging. It consists of tensioning wheels, guide bolts, compression springs, and baffles. The tensioning wheels, under the action of

compression springs, support the sagging tracks, reducing or eliminating slack. When the robot climbs over obstacles and the tracks bend, the deformation of the compression springs increases, but this does not interfere with the robot's ability to traverse obstacles.

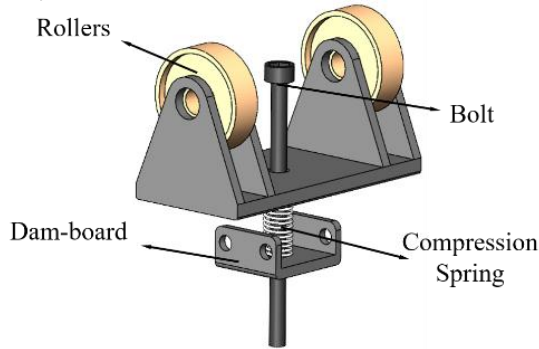


Figure 8. Tensioning mechanism.

3. Mechanical Performance Analysis of the Robot

To ensure the safety and reliability of the robot's operation, its mechanical performance must be analyzed. When the robot rotates around a curved surface, its movement can be approximated as climbing a slope with a certain inclination angle, considering the relatively small size of the robot compared to the curved surface. The varying angle between the robot and the ground significantly alters the force conditions during operation. Therefore, a mechanical model of the robot climbing an inclined surface is established, as shown in Figure 9. Here, $Ox_0y_0z_0$ represents the global coordinate system, and the slope inclination angle θ is variable.

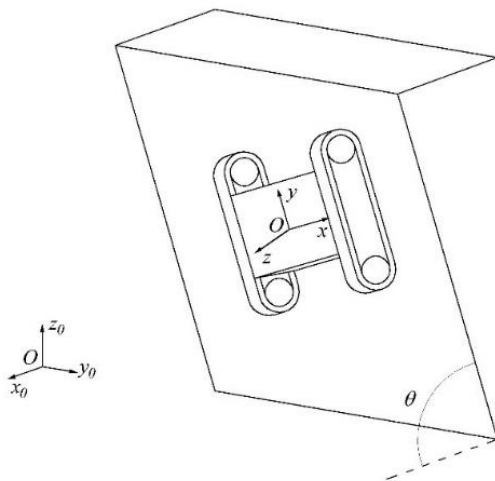


Figure 9. Robot on an inclined surface.

3.1. Static Analysis

During operation, the robot may fail in two primary ways: sliding downward due to gravity when stationary, or the adsorption units detaching sequentially from top to bottom due to the overturning moment caused by gravity [9]. The critical conditions for these two failure types are analyzed below.

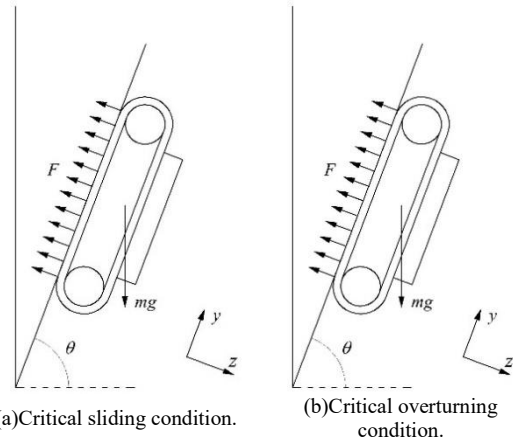


Figure 10. Static analysis of the robot.

3.1.1. Critical Sliding Condition

The primary reasons for the robot sliding downward when stationary are insufficient adsorption force of the units and low friction coefficient between the contact material and the wall surface. When the robot is adsorbed on an inclined wall, as shown in Figure 10, the forces acting on the robot include gravitational force G , the adsorption force F_s , and friction force F_f . For simplicity, only the scenario where the wall inclination angle θ is less than 90° (Figure 10a) is considered, as gravity can provide supportive force increasing friction when θ is greater than 90° .

The components of the robot's gravitational force in the $Oxyz$ coordinate system are

$$\begin{cases} G_x = 0 \\ G_y = G \sin \theta \\ G_z = G \cos \theta \end{cases} \quad (1)$$

Where $G = mg$, m is the total mass of the robot and its load, and g is the acceleration due to gravity.

The friction force is given by

$$F_f = \mu(F_s - G_z) \quad (2)$$

where $F_s = 2nF$, μ is the static friction coefficient, n is the number of track plates in contact with the wall on one side, and F is the adsorption force of a single track plate.

At the critical sliding condition

$$F_f = G_y. \quad (3)$$

Combining these equations, the adsorption force of a single track plate at the critical sliding condition is

$$F = \frac{mg \sin \theta}{2n\mu} + \frac{mg \cos \theta}{2n}. \quad (4)$$

3.1.2. Critical Overturning Condition

Under the influence of gravity, an overturning moment acts on the robot. When the robot begins to overturn, the upper track plates in contact with the wall will detach first, followed sequentially by the others, leading to the robot falling. Based on the torque calculation formula, the overturning moment exerts a larger force on the upper track plates and a smaller force on the lower ones. Additionally, since torque cannot be transmitted between track plates, only the upper and lower plates in contact with the wall are truly effective. Therefore, the upper track plates will detach from the wall first. With the internal load-bearing mechanism, the track plates in contact with the wall jointly resist the overturning moment, as illustrated in Figure 10, showing the critical state of the robot overturning.

The overturning moment due to the robot's gravity is given by

$$M_G = mg \cos \theta \cdot \frac{L}{2} + mg \sin \theta \cdot H \quad (5)$$

where L is the length of the track segment in contact with the wall, and H is the distance from the robot's center of mass to the wall.

The moment resisting the overturning is mainly provided by the track plates in contact with the wall on both sides of the robot. According to the torque calculation formula, the total moment provided by these track plates is

$$M = 2 \cdot \sum_{i=1}^n F \cdot (i-1) \frac{L}{n} \quad (6)$$

At the critical overturning condition

$$M = M_G \quad (7)$$

Combining equations (5) to (7), the adsorption force of a single track plate at the critical overturning state is

$$F = \frac{mg \cos \theta}{2(n-1)} + \frac{mg \sin \theta \cdot H}{(n-1)L} \quad (8)$$

3.2. Dynamic Analysis

In the previous section, we analyze the two instability conditions of the robot in a static state and determined the required adsorption force provided by a single track plate. This section will analyze the robot's straight-line and turning motions on a wall and determine the parameters of the drive device.

3.2.1. Straight-Line Motion State

During straight-line motion, the main sources of resistance for the robot include gravity, the resistance torque generated by lifting the track plates during track movement, and the inertia torque caused by acceleration. When the robot has a certain acceleration, its kinetic energy increases, and gravitational potential energy decreases during downward motion. The energy output by the drive device, along with the decreased gravitational potential energy, contributes to the increase in the robot's kinetic energy. During upward motion, the gravitational potential energy increases, requiring the drive device's output energy to be converted into both kinetic energy and gravitational potential energy. Thus, the drive torque required for upward motion is not less than that for downward motion, so we only need to analyze the upward motion condition. To analyze the forces on the robot during upward straight-line motion, the robot is divided into three parts as shown in Figure 11, where the lower wheel is the driving wheel.

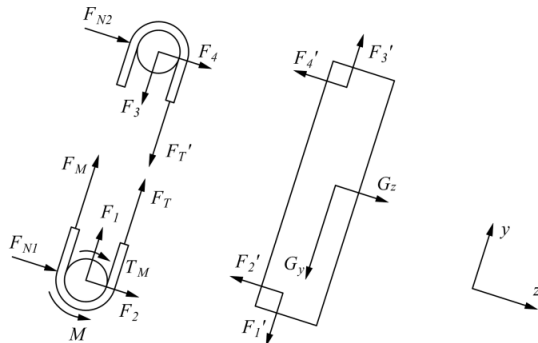


Figure 11. Force analysis of the robot during upward straight-line motion.

The lower wheel is subjected to the drive torque M provided by the drive device, the resistance torque T_M from lifting the adsorption units, the normal force F_{N1} from the

wall, the forces F_1 and F_2 from the robot frame, the track tension F_T , and the circumferential force F_M applied to the lower wheel by the track segment in contact with the wall. The balance equations are

$$\begin{cases} F_{N1} + F_2 = 0 \\ F_1 + F_T + F_M = m_1 a \\ M - T_M + F_T R - F_M R = J_1 \alpha \end{cases} \quad (9)$$

where a is the robot's straight-line acceleration, α is the angular acceleration of the lower wheel, m_1 is the mass of the lower wheel part, J_1 is the rotational inertia of the lower wheel part, and R is the wheel radius.

The upper wheel is subjected to the normal force F_{N2} from the wall, the forces F_3 and F_4 from the robot frame, and the track tension F_T' . The balance equations are

$$\begin{cases} F_{N2} + F_4 = 0 \\ -F_3 - F_T' = m_2 a \\ -F_T' R = J_2 \alpha \end{cases} \quad (10)$$

where m_2 is the mass of the upper wheel part and J_2 is the rotational inertia of the upper wheel part.

The robot frame is subjected to the forces from the upper and lower wheel parts and its weight. The balance equations are

$$\begin{cases} G_z - F_4' - F_2' = 0 \\ F_3' - F_1' - G_y = m_0 a \\ F_1'(H-R) - F_2' \frac{L}{2} - F_3'(H-R) + F_4' \frac{L}{2} = 0 \end{cases} \quad (11)$$

where m_0 is the mass of the robot frame.

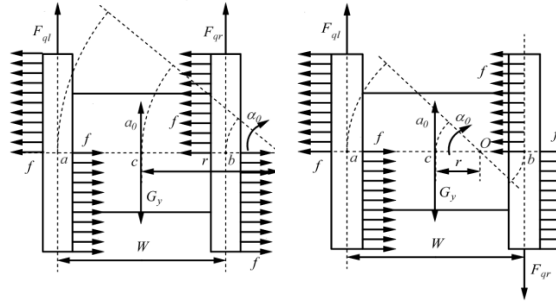
Combining (9) to (11), we get the required drive torque for the robot during upward straight-line motion

$$M = T_M + J \alpha + m a R + m g R \sin(\theta) \quad (12)$$

Turning Motion State

The designed climbing robot turns by differential movement of the tracks on both sides. The turning speed and radius depend on the speeds of the tracks on both sides. When the speed directions of both tracks are the same, the robot rotates around a point outside its body, with a turning radius greater than half the robot's width. When the speed directions are opposite, the robot rotates around a point inside its body, with a smaller turning radius. Taking right turns as an example, these two cases are shown in Figure 12, where O is the robot's turning center, a and b are the center points of the tracks on both sides, c is the robot's body center point, r is the turning radius, W is the robot's body width, v is the turning linear speed, and v_l and v_r are the speeds of the tracks on both sides.

When the climbing robot turns, the resistance torques it experiences include the resistance torque due to the robot body's gravity, the friction torque between the tracks and the wall, and the resistance torque generated by lifting the adsorption units. The force analysis for the robot during turning is shown in Figure 12, where a_0 and α_0 represent the linear and angular accelerations of the robot body center during turning, and F_{ql} and F_{qr} represent the driving forces of the tracks on both sides.



(a) The speed directions on both sides are the same. (b) The speeds on both sides are in opposite directions.

Figure 12. Force analysis of the climbing robot during turning.

The resistance torque due to the robot body's gravity is given by

$$M_G = G_y \cdot r. \quad (13)$$

The friction torque between the tracks and the wall is given by

$$M_f = 2 \sum_{i=1}^n \mu F_{Ni} d_i \quad (14)$$

where F_{Ni} is the normal force exerted by the i -th track plate's adsorption unit on the wall, and d_i is the distance from the i -th track plate's adsorption unit to the track center point. For ease of calculation, assume that each track plate exerts an equal normal force on the wall. In this case, the normal force F_N exerted by a single track plate on the wall can be expressed as

$$F_N = F - \frac{G_z}{2n}. \quad (15)$$

When the speed directions of the tracks on both sides are the same, the driving torque for turning is

$$M_q = F_{ql} \left(r + \frac{W}{2} \right) + F_{qr} \left(r - \frac{W}{2} \right). \quad (16)$$

The balance equations for the entire robot are

$$\begin{cases} F_{ql} + F_{qr} - G_y = ma_0 \\ M_q - M_G - M_f = J_0 \alpha_0 \end{cases} \quad (17)$$

where J_0 is the rotational inertia of the climbing robot around the turning center. Combining equations (13), (16), and (17), the driving forces F_{ql} and F_{qr} for the tracks on both sides can be derived as

$$\begin{cases} F_{ql} = \frac{G_y}{2} - \frac{ma_0 \left(r - \frac{W}{2} \right)}{W} + \frac{J_0 \alpha_0 + M_f}{W} \\ F_{qr} = \frac{G_y}{2} + \frac{ma_0 \left(r + \frac{W}{2} \right)}{W} - \frac{J_0 \alpha_0 + M_f}{W} \end{cases} \quad (18)$$

When the speed directions of the tracks on both sides are opposite, the driving torque for turning is

$$M_q = F_{ql} \left(r + \frac{W}{2} \right) + F_{qr} \left(\frac{W}{2} - r \right). \quad (19)$$

The dynamic balance equations for the entire robot are

$$\begin{cases} F_{ql} - F_{qr} - G_y = ma_0 \\ M_q - M_G - M_f = J_0 \alpha_0 \end{cases} \quad (20)$$

Combining equations (13) and (19) into (20), the driving forces for the tracks on both sides are

$$\begin{cases} F_{ql} = \frac{J_0 \alpha_0 + M_f}{W} + \frac{G_y}{2} + \frac{ma_0 \left(\frac{W}{2} - r \right)}{W} \\ F_{qr} = \frac{J_0 \alpha_0 + M_f}{W} - \frac{G_y}{2} - \frac{ma_0 \left(r + \frac{W}{2} \right)}{W} \end{cases} \quad (21)$$

By analyzing equations (18) and (21), it is evident that regardless of whether the speed directions of the tracks on both sides are the same, the driving force on the left track is

greater than that on the right track. The expression for the driving force on the left track is the same, but the value of r changes, resulting in a positive or negative $\frac{W}{2} - r$. Therefore, when the robot turns left with a turning radius of 0, the left track's driving force is maximized. The maximum driving force F_{qmax} is

$$F_{qmax} = \frac{G_y + ma_0}{2} + \frac{J_0 \alpha_0 + M_f}{W}. \quad (22)$$

When the speed directions of the tracks on both sides are opposite, the driving torque is

$$M_q = F_{ql} \left(r + \frac{W}{2} \right) + F_{qr} \left(\frac{W}{2} - r \right). \quad (23)$$

Combining equations (1), (14), and (15), we obtain

$$M = \frac{mg \cos \theta + ma_0}{2} R + \frac{J_0 \alpha_0}{W} R + \frac{2\mu n F - \mu mg \cos \theta}{n} R \sum_{i=1}^n d_i + T_M + J_1 \alpha_1. \quad (24)$$

3.3. Numerical Calculation

Based on the previous analysis of the critical conditions for the climbing robot's slip instability and overturning instability, to ensure that the robot can stably adhere to the wall, the minimum adsorption force for a single track plate should be the maximum value from equations (4) and (8). To determine the adsorption force of a single track plate, we perform numerical calculations using MATLAB. Inspired by [40], the requirements of total mass of the robot body and load $m = 50kg$. According to the design of the robot, the length of the contact section between the track and the wall $L = 300mm$, the distance from the center of mass to the wall $H = 120mm$, the Number of track plates in contact with the wall on one side $n = 10$. Assume the static friction coefficient between the contact material and the wall $\mu = 0.6$. The relationship curve between the adsorption force of a single track plate and the wall angle is shown in Figure 13.

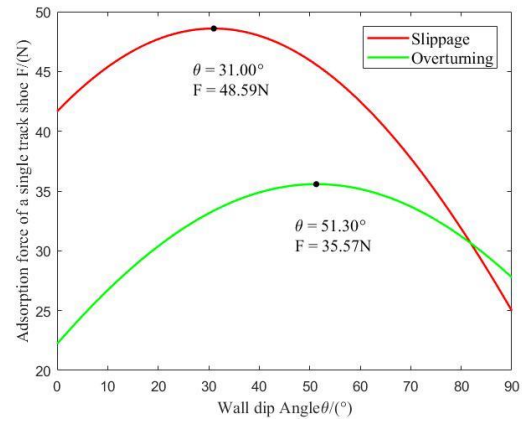


Figure 13. Adsorption force of a single track shoe

The adsorption force required for the robot to resist slip instability reaches its maximum at a wall angle of 31° , while the adsorption force required to resist overturning instability reaches its maximum at 51.3° . When the wall angle is less than 80° , the primary form of instability for the robot is slip instability. When the wall angle approaches 90° , overturning instability becomes the main form of instability. To ensure the robot can stably adhere to the wall, the adsorption force of a single track plate should be no less than $48.59N$. For safety, the adsorption force of a single

track shoe is set to 55N. Each track plate of the robot in this paper has two adsorption units. If the adsorption unit's magnetic force could be 27.5N, the magnetic force of the track shoe will be 55N.

To ensure that the climbing robot can move flexibly on curved surfaces, the required driving torque of the robot's drive device is calculated. According to the design of the robot, the width of the robot is $W = 377\text{mm}$, the radius of the drive wheel $R = 50\text{mm}$. Assume the rotational inertia of the robot around the turning center $J_0 = 10\text{kg} \cdot \text{m}^2$, the rotational inertia of the drive wheel $J_1 = 0.05\text{kg} \cdot \text{m}^2$, the resistance torque generated by lifting a single track plate $T_M = 5\text{kg} \cdot \text{m}^2$, the robot's acceleration during straight motion is 0.1m/s^2 , and the angular acceleration of the drive wheel is 2rad/s^2 . When turning, both the linear acceleration of the robot and the angular acceleration of the drive wheel are zero. The driving torque M and angle θ during straight and turning motions are calculated using MATLAB, as shown in Figure 14.

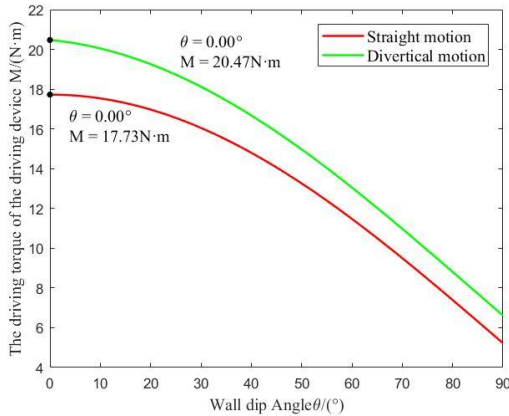


Figure 14. The driving torque of the driving device

From the calculations: The required driving torque for straight motion and turning both reach their maximum at $\theta = 0^\circ$. The driving torque required for turning is always greater than that required for straight motion. To ensure the robot can move flexibly on the wall, the driving torque provided by the drive device on one side of the track should be greater than $20.47\text{N} \cdot \text{m}$.

4. Simulation Analysis

After completing the structural design of the climbing robot, simulation analysis is conducted using virtual prototyping technology. This approach helps identify defects and shortcomings promptly. Optimizing the robot based on simulation results can effectively save costs and shorten the development cycle.

4.1. Adhesion Force Calculation

The permanent magnet used is made of NdFeB, a hard and brittle material, in the form of a $5\text{mm} \times 5\text{mm} \times 5\text{mm}$ cube.

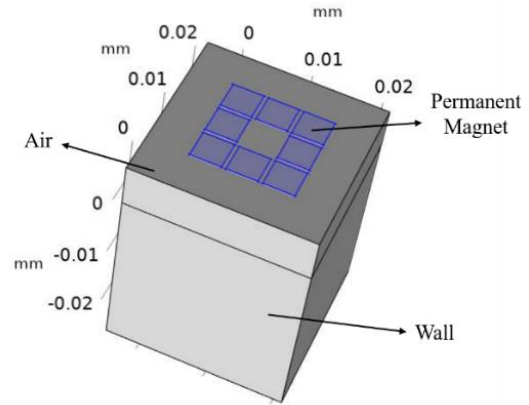


Figure 15. COMSOL simulation model.

The total force on a charged particle within an object due to an electromagnetic field can be obtained by integrating the following equation

$$f = \epsilon_0(\nabla \cdot E)E + \frac{1}{\mu_0}(\nabla \times B) \times B - \epsilon_0 \frac{\partial E}{\partial t} \times B. \quad (25)$$

For calculating the adhesion force of the permanent magnet, the electric field can be ignored, making the first and third terms zero. Using COMSOL simulation, the adhesion forces of NdFeB permanent magnets of grades N52, N42, and N35 were calculated. To simulate a real work situation, the air gap is set to 1.2mm, the wall material is set to S350 with a maximum relative permeability of 850 and its thickness are 26mm. In Figure 15, the purple area represents the permanent magnet, the area below is the wall and the rest is air. The calculated adhesion forces on the wall are shown in Table 1.

Table 1. Adhesion force of different magnet grades.

Grade	Type	Adhesion force (N)
N52	Halbach array	33.057
N42	Halbach array	27.812
	Ordinary	9.213
N35	Halbach array	23.402

From the static analysis, it is determined that for the robot to stably adhere to a curved surface, the adhesion force provided by the unit on a single track plate should exceed 55N. In the design of the robot, every track shoe of the robot in this paper has two adsorption units. Then, if an adsorption unit's magnetic force could be 27.5N, the magnetic force of a track shoe will be 55N. According to Table 1, the adsorption force of the square Halbach array using N42 is 27.812N. Therefore, N42 permanent magnets are selected for the adhesion unit.

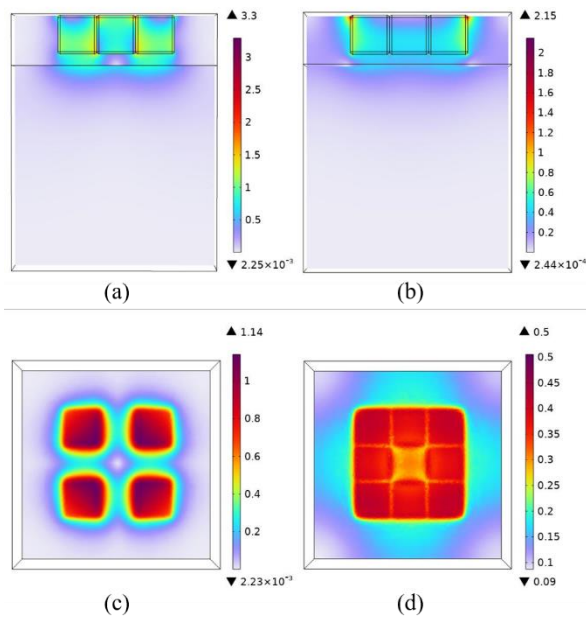


Figure 16. COMSOL simulation results: (a) Magnetic induction intensity of N42 permanent magnet Halbach array (front view), (b) Magnetic induction intensity of N42 permanent magnet with parallel arrangement (front view), (c) Magnetic induction intensity of N42 permanent magnet Halbach array (top view), (d) Magnetic induction intensity of N42 permanent magnet with parallel arrangement (top view).

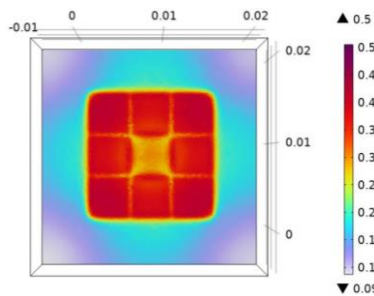


Figure 17. COMSOL simulation results of ordinary adsorption devices (N42)

From Figure 16 and Figure 17, it can be seen that the magnetic induction intensity at the edges of the Halbach array is smaller. Compared to the parallel arrangement of permanent magnets, the magnetic induction intensity beneath the adhesion unit is larger and more concentrated. The Halbach array's magnetic adhesion force is primarily concentrated at the corners, while the force is more uniformly distributed in the parallel arrangement. The Halbach array enhances the magnetic field effect and improves the utilization of the permanent magnet's magnetic energy.

4.2. Axial Movement of the Track

The robot track model is established in SOLIDWORKS and imported into ADAMS for virtual simulation. During the simulation, the track started to move at 0.5s and stopped at 3s, as shown in Figure 18. Figure 19 is the curve of the track center of mass position changing with time. It can be found that under the action of the tensioning mechanism, the track is relaxed and shaken to a very small extent.

In the first 0.5s of the simulation, the track does not move, but due to gaps between parts and the effect of

gravity, the acceleration of the track's center of mass fluctuates slightly. At 0.5s, the rear wheels start to rotate, but the acceleration of the center of mass does not increase synchronously, as shown in Figure 20. During the track's movement, the acceleration continuously fluctuates, and larger fluctuations occur when the center of mass speed is higher. This is because the rear wheels drive the track, and gaps between parts cause asynchronous movement between the rear wheels and the track. The transmission between the rear wheels and the track plates is achieved through contact forces. The rotation of the drive wheels causes the track plates to experience impact movements, leading to continuous fluctuations in the acceleration of the track's center of mass. When the speed of the drive wheels is higher, they carry greater momentum, resulting in larger changes in the acceleration of the track's center of mass. Therefore, increasing the assembly precision to reduce gaps between parts and increasing the overall mass of the track plates should be considered to achieve smoother transmission and reduce acceleration fluctuations.

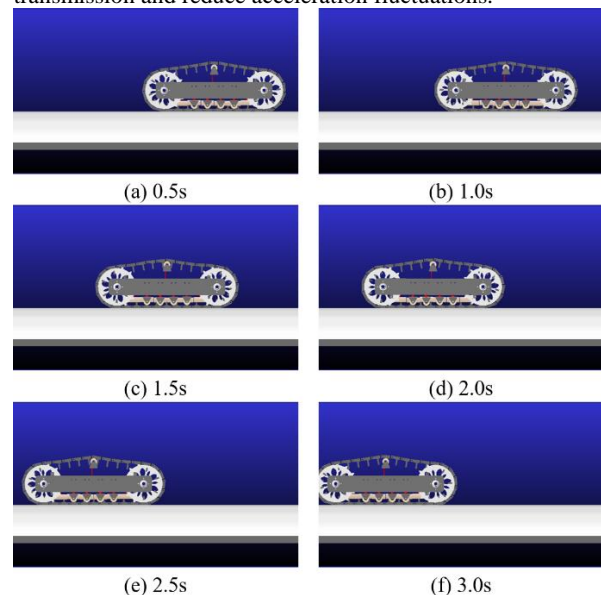


Figure 18. Axial movement simulation.

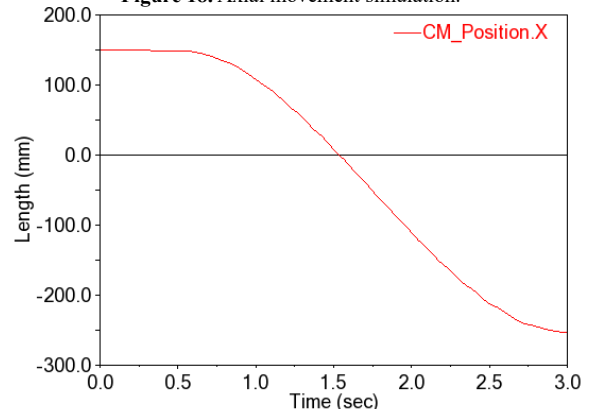


Figure 19. Time-position curve of the center of mass.

During the axial movement of the track along the wall, as shown in Figure 21, the track's acceleration is relatively high between 1.25s and 2s, resulting in increased track tension. At other times, the track tension fluctuates around 12.5N.

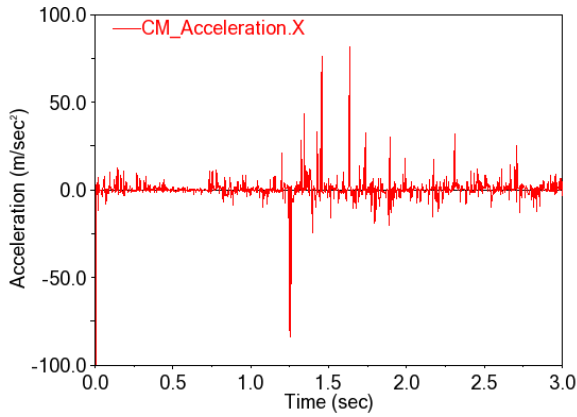


Figure 20. Time-acceleration curve of the center of mass.

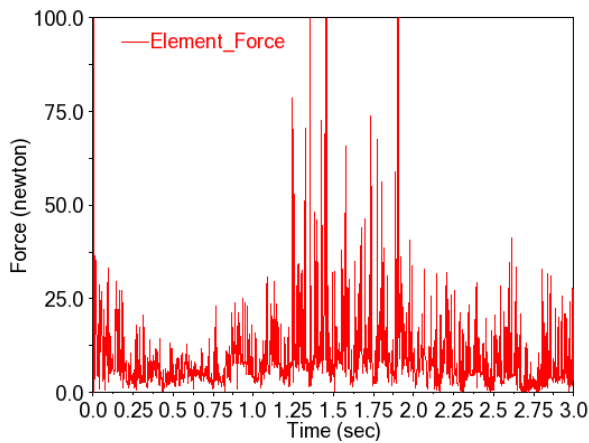


Figure 21. Track tension

4.3. Circumferential Movement of the Track

The simulation of the track moving along the curved surface's axial direction is shown in Figure 22. The total simulation time is set to 3s with 300 simulation steps, but the analysis is conducted only for the first 2s since the track exceeded the wall's range at approximately 1.7s. Figure 23 shows the displacement-time curves of the center of mass in the x and z directions during circumferential movement. The simulation results indicate good conformity between the track and the curved wall surface. The rear side of the track do not detach from the wall when contacting the wall's edge, demonstrating the track's obstacle-crossing capability.

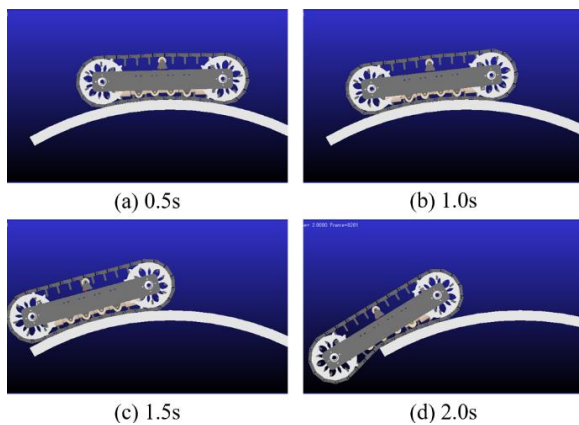


Figure 22. Axial movement simulation.

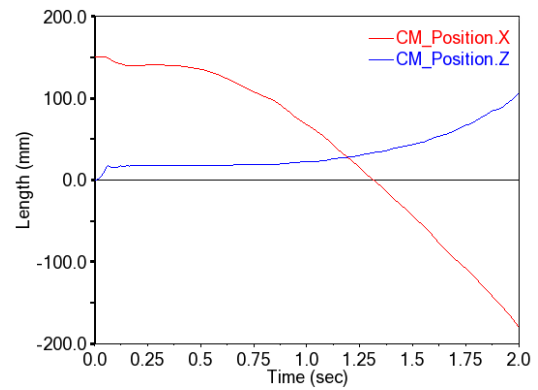
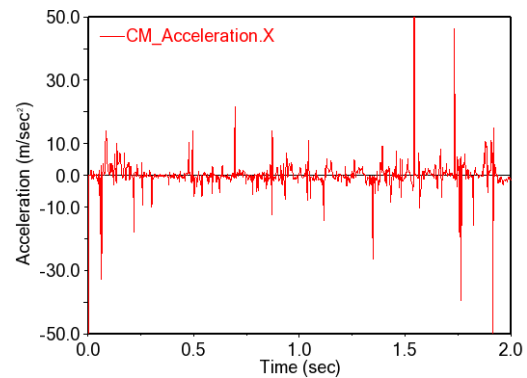
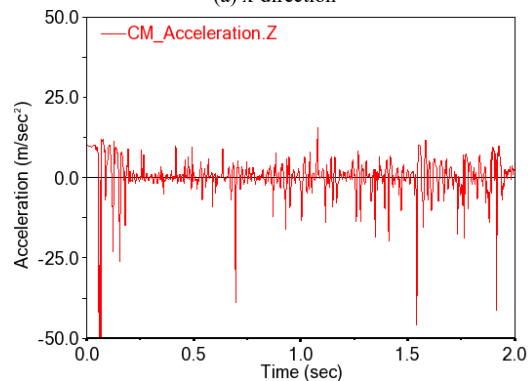


Figure 23. Time-displacement curve of the center of mass.



(a) x-direction



(b) z-direction

Figure 24. Time-acceleration curve of the center of mass.

Before the drive wheel starts rotating at 0.3s, the position of the track's center of mass changes in both the x and y directions due to gaps between parts. These gaps cause non-uniform changes in the center of mass position, which are more pronounced in the z-direction. Figure 24 shows the acceleration-time curves of the center of mass in the x and z directions. In the first 0.3s, the acceleration fluctuates, with greater fluctuations in the z direction and remaining above zero for a certain period. This indicates that gaps between parts cause more significant position changes of the track's center of mass in the z direction compared to the x direction. After 1.5s, significant fluctuations in the acceleration of the center of mass occur in both the x and z directions as the track reaches the wall's edge and begins to contact the wall's corner. This suggests that while the track has some obstacle-crossing capability, significant impacts occur during this process. Increasing the track length or reducing the width of the track plates could be considered as improvements.

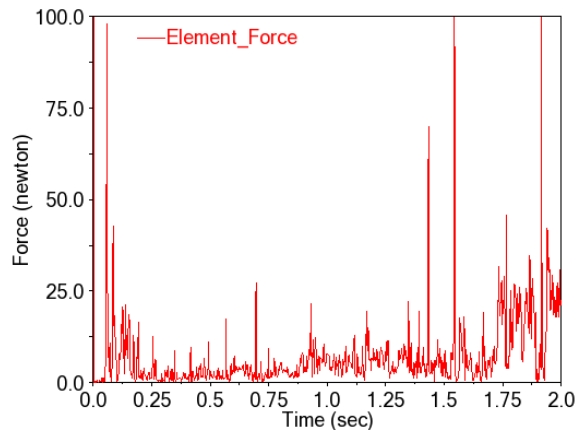


Figure 25. Track tension

As shown in Figure 25, during the circumferential movement of the track along the wall, the gaps between the track components result in increased tension at the beginning of the simulation, causing greater interaction forces between the track plates. After 1.5s, the track reaches the edge of the wall and begins to contact the wall corner, leading to a significant increase in track tension.

5. Conclusion and Outlook

This paper presents the design of a track-based climbing robot utilizing a Halbach array magnetic configuration. The adhesion units are arranged using a Halbach square magnetic array of permanent magnets. The designed load-bearing mechanism directly transfers the robot's weight to the track plates, while the tensioning mechanism supports the slack track, reducing energy loss due to slack vibration during movement.

Static analysis revealed that the maximum adhesion force required for a single track plate to resist slip instability occurs at a wall angle of 31° , and the maximum adhesion force required to resist overturning instability occurs at 51.3° . The robot predominantly experiences slip instability at wall angles less than 80° , while overturning instability becomes the primary form of instability as the wall angle approaches 90° . To ensure stable adhesion to the wall, the adhesion force of a single track plate should be no less than 48.59N.

Dynamic analysis shows that the driving torque required for the climbing robot to move straight and to turn on the wall reaches its maximum at $\theta=0^\circ$. The driving torque required for turning is consistently greater than that required for straight movement. During motion simulation, the track segment in contact with the wall adheres well, and the slack segment exhibits minimal vibration. However, fluctuations in the robot's acceleration are observed during movement, particularly at higher speeds and when the wall surface is uneven. These fluctuations are likely due to gaps between the robot's components, which can be mitigated by improving precision to reduce gaps, increasing the total mass of the track plates, extending the track length, and reducing the width of the track plates.

Future research will focus on designing a control algorithm for the climbing robot and testing the robot's performance on a prototype through practical experiments.

Declaration of conflicting interests

The author(s) declared no potential conflicts of interest with respect to the research, authorship, and /or publication of this article.

Acknowledgments

This work was supported in part by the Key R&D Program of Guangxi Province under Grant GKAB23026101, in part Guangxi Natural Science Foundation under Grant 2023GXNSFBA026287, in part Guangxi Natural Science Foundation under Grant 2020JJB160014, and in part Guangxi Postdoctoral Innovative Talent Support Program.

References

- [1] J. Gong, W. Wei, S. Peng, K. Zhang, "Analytical formula of positive position solution of 2PPA-PSS 3-translational parallel mechanism with low coupling-degree and its numerical application", *Jordan Journal of Mechanical and Industrial Engineering*, Vol. 28, No. 33, 2021, pp.419-429. https://jjmie.hu.edu.jo/vol15-5/02-jjmie_41_21.pdf.
- [2] H. A. Y. Maldonado, "Design, study, and comparison of a new axial fan using the fibonacci spiral and a classic axial fan", *Jordan Journal of Mechanical and Industrial Engineering*, Vol. 81, No.1, 2024, pp.75-87. <https://doi.org/10.59038/jjmie/180106>.
- [3] B. Zhao, "Multi-layer and multi-channel welding trajectory control method of welding robot", *Jordan Journal of Mechanical and Industrial Engineering*, Vol. 16, No. 1, 2022, pp.153-162. <https://jjmie.hu.edu.jo/vol16-1/17-jjmie-J679.pdf>.
- [4] M. Soori, M. Asmael, "A review of the recent development in machining parameter optimization", *Jordan Journal of Mechanical and Industrial Engineering*, Vol. 16, No. 2, 2022, pp.205-223. <https://hal.science/hal-03588524/document>.
- [5] J. Li, "Distributed multi-level inventory algorithms for automotive maintenance spare parts based on centralized control model", *Jordan Journal of Mechanical and Industrial Engineering*, Vol. 14, No. 1, 2020, pp.89-99. <https://jjmie.hu.edu.jo/VOL-14-1/11-jjmie-440-01.pdf>.
- [6] S. Kim, M. Spenko, S. Trujillo, B. Heyneman, D. Santos, M. R. Cutkosky, "Smooth vertical surface climbing with directional adhesion", *IEEE Transactions on Robotics*, Vol. 24, No. 1, 2008, pp.65-74. <https://doi.org/10.1109/TRO.2007.909786>.
- [7] N. Gravish, M. Wilkinson, S. Sponberg, A. Parness, N. Esparza, D. Soto, T. Yamaguchi, M. Broide, M. Cutkosky, C. Creton, K. Autumn, "Rate-dependent frictional adhesion in natural and synthetic gecko setae", *Journal of The Royal Society Interface*, Vol. 7, No. 43, 2010, pp.259-269. <https://doi.org/10.1098/rsif.2009.0133>.
- [8] H. Choi, M. R. Cutkosky, A. A. Stanley, "Integrated pneumatic sensing and actuation for soft haptic devices", *IEEE Robotics and Automation Letters*, Vol. 8, No. 11, 2023, pp.7591-7598. <https://doi.org/10.1109/LRA.2023.3320494>.
- [9] A. Hajj-Ahmad, L. Kaul, C. Matl, M. Cutkosky, "GRASP: Grocery robot's adhesion and suction picker", *IEEE Robotics and Automation Letters*, Vol. 8, No. 10, 2023, pp.6419-6426. <https://doi.org/10.1109/LRA.2023.3300572>.
- [10] A. K. Han, A. Hajj-Ahmad, M. R. Cutkosky, "Bimanual handling of deformable objects with hybrid adhesion", *IEEE Robotics and Automation Letters*, Vol. 7, No. 2, 2022, pp.5497-5503. <https://doi.org/10.1109/LRA.2022.3158231>.
- [11] H. Li, Y. Bu, Y. Bu, S. Mao, Y. Guan, H. Zhu, "Design and control of a transformable multi-mode mobile robot", *IEEE*

- Robotics and Automation Letters, 2023, pp.1302-1309. <https://doi.org/10.1109/LRA.2023.3344352>.
- [12] Y. Guan, H. Zhu, W. Wu, X. Zhou, L. Jiang, C. Cai, L. Zhang, H. Zhang, "A modular biped wall-climbing robot with high mobility and manipulating function", IEEE/ASME Transactions on Mechatronics, Vol. 18, No. 6, 2012, pp.1787-1798. <https://doi.org/10.1109/TMECH.2012.2213303>.
- [13] H. Zhu, J. Lu, S. Gu, S. Wei, Y. Guan, "Planning three-dimensional collision-free optimized climbing path for biped wall-climbing robots", IEEE/ASME Transactions on Mechatronics, Vol. 26, No. 5, 2020, pp.2712-2723. <https://doi.org/10.1109/TMECH.2020.3045089>.
- [14] S. Gu, H. Zhu, X. Lin, J. Tan, W. Ye, Y. Guan, "Truss member registration for implementing autonomous gripping in biped climbing robots", Automation in Construction, Vol. 136, 2022, pp.104146. <https://doi.org/10.1016/j.autcon.2022.104146>.
- [15] Q. Fu, Y. Guan, H. Zhu, "A novel robot with rolling and climbing modes for power transmission line inspection", 2022 IEEE/RSJ International Conference on Intelligent Robots and Systems (IROS), Kyoto, Japan, 2022: 7122-7128. <https://doi.org/10.1109/IROS47612.2022.9981434>.
- [16] J. Liu, L. Xu, S. Chen, H. Xu, G. Cheng, J. Xu, "Development of a bio-inspired wall-climbing robot composed of spine wheels, adhesive belts and eddy suction cup", Robotica, Vol. 39, No. 1, 2021, pp.3-22. <https://doi.org/10.1017/S026357471900184X>.
- [17] W. Wang, X. Wang, G. Zheng, R. Chen, Z. Yuan, J. Huang, K. Wu, G. Bao, "A modular soft pipe-climbing robot with high maneuverability", IEEE/ASME Transactions on Mechatronics, 2024, <https://doi.org/10.1109/TMECH.2024.3385506>.
- [18] R. Chen, L. Fu, Y. Qiu, R. Song, Y. Jin, "A gecko-inspired wall-climbing robot based on vibration suction mechanism", Proceedings of the Institution of Mechanical Engineers, Part C: Journal of Mechanical Engineering Science, Vol. 233, No. 19-20, 2019, pp.7132-7143. <https://doi.org/10.1177/0954406219869041>.
- [19] Y. Liu, L. Wang, F. Niu, P. Li, Y. Li, T. Mei, "A track-type inverted climbing robot with bio-inspired spiny grippers", Journal of Bionic Engineering, Vol. 17, 2020, pp.920-931. <https://doi.org/10.1007/s42235-020-0093-5>.
- [20] Y. Liu, S. Liu, L. Wang, X. Wu, Y. Li, T. Mei, "A novel tracked wall-climbing robot with bio-inspired spine feet", Intelligent Robotics and Applications: 12th International Conference, Shenyang, China, 2019. https://doi.org/10.1007/978-3-030-27532-7_8.
- [21] Q. Zhao, Z. Jiang, H. K. Chu, "A soft-rigid air-propelled pipe-climbing robot", 2021 IEEE International Conference on Robotics and Automation (ICRA). IEEE, 2021. <https://doi.org/10.1109/ICRA48506.2021.9561321>.
- [22] Y. Liu, L. He, S. Yuan, "Wear properties of aluminum alloy 211z. 1 drilling tool", Jordan Journal of Mechanical and Industrial Engineering, Vol. 15, No. 1, 2021, pp.59-63. <https://jjmie.hu.edu.jo/v15-1/08-ST2617.pdf>.
- [23] S. Sahu, S. P. Jena, "Application of hybrid fuzzy technique for damage estimation in structural member", Jordan Journal of Mechanical and Industrial Engineering, Vol. 17, No. 2, 2023, pp.195-204. <https://doi.org/10.59038/jjmie/170204>.
- [24] Y. Yoshida, S. Ma, "Design of a wall-climbing robot with passive suction cups", 2010 IEEE International Conference on Robotics and Biomimetics. IEEE, 2010. <https://doi.org/10.1109/ROBIO.2010.5723554>.
- [25] K. Cao, G. Qin, J. Zhou, J. Xu, L. Xu, A. Ji, "Design and experimental research of a rolling-adsorption wall-climbing robot", Industrial Robot: The International Journal of Robotics Research and Application, Vol. 51, No. 2, 2024, pp.258-268. <https://doi.org/10.1108/IR-08-2023-0194>.
- [26] J. Zhao, X. Li, J. Bai, "Experimental study of vortex suction unit-based wall-climbing robot on walls with various surface conditions", Proceedings of the Institution of Mechanical Engineers, Part C: Journal of Mechanical Engineering Science, Vol. 232, No. 21, 2018, pp.3977-3991. <https://doi.org/10.1177/0954406218791203>.
- [27] J. Liu, L. Xu, J. Xu, L. Liu, G. Cheng, S. Chen, H. Xu, J. Shi, X. Liang, "Analysis and optimization of the wall-climbing robot with an adsorption system and adhesive belts", International Journal of Advanced Robotic Systems, Vol. 17, No. 3, 2020, pp.1729881420926409. <https://doi.org/10.1177/1729881420926409>.
- [28] W. Song, H. Jiang, T. Wang, D. Ji, S. Zhu, "Design of permanent magnetic wheel-type adhesion-locomotion system for water-jetting wall-climbing robot", Advances in Mechanical Engineering, Vol. 10, No. 7, 2018, pp.1687814018787378. <https://doi.org/10.1177/1687814018787378>.
- [29] K. Thung-Od, K. Kanjanawanishkul, T. Maneewarn, T. Sethaput, A. Boonyaprapasorn, "An in-pipe inspection robot with permanent magnets and omnidirectional wheels: Design and implementation", Applied Sciences, Vol. 12, No. 3, 2022, pp.1226. <https://doi.org/10.3390/app12031226>.
- [30] B. Zhao, "Multi-layer and multi-channel welding trajectory control method of welding robot", Jordan Journal of Mechanical & Industrial Engineering, Vol. 16, No.1, 2022, pp.153-162. <https://jjmie.hu.edu.jo/vol16-1/17-jjmie-J679.pdf>.
- [31] P. Zhao, "Moving trajectory tracking method of multi degree of freedom manipulator based on particle filter algorithm", Jordan Journal of Mechanical & Industrial Engineering, Vol. 16, No. 4, 2022, pp.591-600. <https://jjmie.hu.edu.jo/vol-16-4/12-174-22.pdf>.
- [32] J. Guo, Y. Lv, H. Zhang, "Coordinated gait control of snake like robot based on electromechanical tracking", Jordan Journal of Mechanical and Industrial Engineering, Vol. 16, No. 1, 2022, pp.87-95. <https://jjmie.hu.edu.jo/vol16-1/JJMIE-2022-16-1.pdf>.
- [33] C. Kuang, X. Zheng, "Space trajectory planning of electric robot based on unscented Kalman filter", Jordan Journal of Mechanical and Industrial Engineering, Vol. 15, No. 1, 2021, pp.29-38. <https://jjmie.hu.edu.jo/v15-1/05-J643.pdf>.
- [34] J. Gong, S. Guo, H. Shen, W. Wei, Y. Long, "Path-tracking cascade control of hydraulic-tracked vehicles based on port-controlled Hamiltonian model", IEEE Transactions on Intelligent Vehicles, <https://doi.org/10.1109/TIV.2024.3417213>.
- [35] J. Hu, X. Han, Y. Tao, S. Feng, "A magnetic crawler wall-climbing robot with capacity of high payload on the convex surface", Robotics and Autonomous Systems, Vol. 148, 2022, pp.103907. <https://doi.org/10.1016/j.robot.2021.103907>.
- [36] Z. Zhao, Y. Tao, J. Wang, J. Hu, "The multi-objective optimization design for the magnetic adsorption unit of wall-climbing robot", Journal of Mechanical Science and Technology, Vol. 36, No. 1, 2022, pp.305-316. <https://doi.org/10.1007/s12206-021-1228-2>.
- [37] F. Gao, J. Fan, L. Zhang, J. Jiang, S. He, "Magnetic crawler climbing detection robot basing on metal magnetic memory testing technology", Robotics and Autonomous Systems, Vol. 125, 2020, pp.103439. <https://doi.org/10.1016/j.robot.2020.103439>.
- [38] E. Abdelsalam, F. Kafiah, S. Kiswani, D. Ibrahim, G. Al, "MFL based prototype and experimental work for detection of defects in cables of bridge structures", Jordan Journal of Mechanical and Industrial Engineering, Vol. 14, No. 4, 2020, pp.361-370. <https://jjmie.hu.edu.jo/vol14-4/JJMIE-2020-14-4.pdf>.
- [39] J. Gong, G. Cai, W. Wei, K. Zhang, S. Peng, "Research on the residual vibration suppression of a controllable mechanism

- robot”, IEEE Access, Vol. 10, 2022, pp.39436-39455. <https://doi.org/10.1109/ACCESS.2022.3165053>.
- [40] Y. Wang, X. Zhang, M. Zhang, L. Sun, M. Li, “Self-compliant track-type wall-climbing robot for variable curvature façade”, IEEE Access, Vol. 10, 2021, pp.51951-51963. <https://doi.org/10.1109/ACCESS.2021.3068000>.
- [41] P. Yang, L. Sun, M. Zhang, “Design and analysis of a passive adaptive wall-climbing robot on variable curvature ship facades”, Applied Ocean Research, Vol. 143, 2024, 103879. <https://doi.org/10.1016/j.apor.2024.103879>.